ACS OMEGA

http://pubs.acs.org/journal/acsodf
Article

Multicomponent Co_2O_3@$CoMo_2S_4$ Core−Shell Structures as a Binder-Free Electrode for Cycling Stability Supercapacitors

Meilong Wang, Linsong Li, Zhentao Liu, Fuzhong Wu, Huixin Jin,* Yi Wang,* and Siyu Cai

Cite This: *ACS Omega* 2025, 10, 8901−8910
Read Online

ABSTRACT: Transitional bimetallic sulfides have garnered significant interest due to their versatile redox reactions, strong electrochemical activity, and cost-effectiveness. However, their low energy density and poor rate performance have hindered their use in energy storage systems. To overcome these challenges, we have developed a Co_2O_3@$CoMo_2S_4$ core−shell structure using a strategic design approach, serving as a conductive framework for supercapacitors. The innovative Co_2O_3@$CoMo_2S_4$ core−shell structure exhibits exceptional performance, achieving a specific capacitance of 4951.8 F g^{-1} at 1 A g^{-1} and retaining 90.85% cyclic stability after 5500 cycles, outperforming most reported transitional bimetallic sulfides. The Co_2O_3@$CoMo_2S_4$//AC supercapacitor achieves an energy density of 41.66 Wh kg^{-1} and a power density of 0.35 kW kg^{-1}. Our research paves the way for the development of transitional bimetallic sulfides with core−shell structures that offer superior performance in supercapacitor applications, providing valuable insights for future advancements in the field.

1. INTRODUCTION

The increased attention worldwide toward renewable energy sources is a result of the widespread reliance on fossil fuels and growing environmental concerns.[1−3] Supercapacitors excel in the competitive energy storage device market due to their impressive power density, quick charge/discharge capabilities, and exceptional cycling stability.[4−8] The efficacy of supercapacitors is significantly influenced by the choice and composition of electrode materials.[9−13]

Transition metal compounds and their hybrid materials are often used as electrode materials in energy storage devices due to their high theoretical specific capacity, which originates from Faradaic redox reactions.[14−19] Transition metal sulfides have shown increased redox activity and higher theoretical capacitance performance compared to transition metal oxides in various electrochemically active materials, which is attributed to the higher electronegativity of sulfur compared to oxygen.[20−22]

Various bimetallic sulfides, such as $NiCo_2S_4$,[23] $CoNi_2S_4$,[24] $CuCo_2S_4$,[25] $FeCo_2S_4$,[26] and $MnCo_2S_4$,[27] are being investigated for their potential as supercapacitor electrode materials. Current research is focused on the synthesis, morphology, structure, and properties of these sulfides. For example, Zhang et al.[28] studied $CuCo_2S_4$ as an anode material in hybrid supercapacitors, achieving an energy output of 51.8 W h/kg and a power output of 700 W/kg using activated charcoal. Additionally, Jing et al.[29] synthesized $CoNi_2S_4$ nanosheets integrated with S,P-doped graphene, achieving a specific capacitance of 1136.5 F g^{-1} (126.28 mA h g^{-1}) at 2 A g^{-1}. Currently, there are limited studies on Co−Mo−S (CMS) BTMSs.[30−32] Theoretically, CMS containing $Co^{2+}/^{3+}$ and $Mo^{4+}/^{6+}$ redox pairs is predicted to be a cost-effective and environmentally friendly candidate for electrode materials in SCs.[33,34] Recent studies have emphasized advancements in CMS. For example, Liu et al. reported the $CoMo_2S_4$@ZnCo−S electrode materials demonstrated a high capacity of 4630 mF/cm^2 at 1 mA/cm^2 and exhibited excellent cycling stability, retaining 85.6% of their capacity after 6000 cycles at 10 mA/cm^2.[35] Yang et al. reported that the Co_3S_4/$CoMo_2S_4$ electrode demonstrates a capacitance of 1457.8 F g^{-1} at 1 A g^{-1} and retains 97% of its initial capacitance after 2000 cycles, indicating excellent stability. Nwaji et al.[36] demonstrated that Co_3S_4@$CoMo_2S_4$ exhibited a high specific capacitance of 980.3 F g^{-1} at 1 A g^{-1}, with a capacity retention of 96.5% after 6000 cycles at 10 A g^{-1}.[37] The complexity of most synthesis processes often increases the phase interface between materials, leading to higher resistance due to composite formation. Thus, employing a cost-effective and simple fabrication method is crucial for producing hybrid electrodes with optimal spatial structures to enhance the $CoMo_2S_4$ efficiency.

This study presents a novel core−shell structure of Co_2O_3@$CoMo_2S_4$ synthesized on Ni foam through a straightforward solution-based technique. The unique core−shell architecture of Co_2O_3@$CoMo_2S_4$ offers an increased number of reactive sites, resulting in a specific capacitance of 4951.8 F g^{-1} at 1 A g^{-1} and demonstrating exceptional durability with 90.85% capacity retention after 5500 cycles, surpassing many previously documented bimetallic sulfides. The asymmetric supercapacitor utilized the optimal combination as the cathode and commercial activated carbon (AC) as the anode. Electrochemical techniques, including cyclic voltammetry, galvanostatic charge−discharge, and electrochemical impedance spectrosco-

Received: June 2, 2024
Revised: February 16, 2025
Accepted: February 21, 2025
Published: February 28, 2025

https://doi.org/10.1021/acsomega.4c05172
ACS Omega 2025, 10, 8901−8910

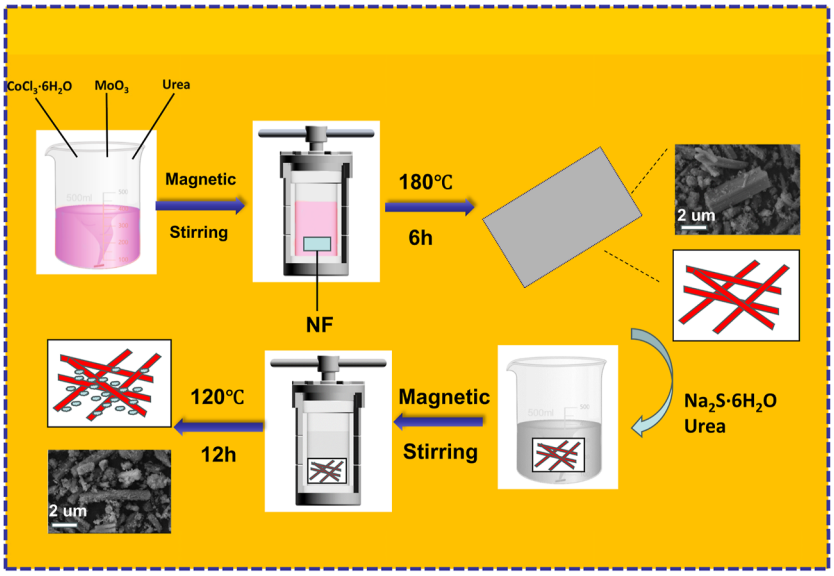

Figure 1. Synthesis the Co_2O_3@$CoMo_2S_4$ flowchart on nickel foam.

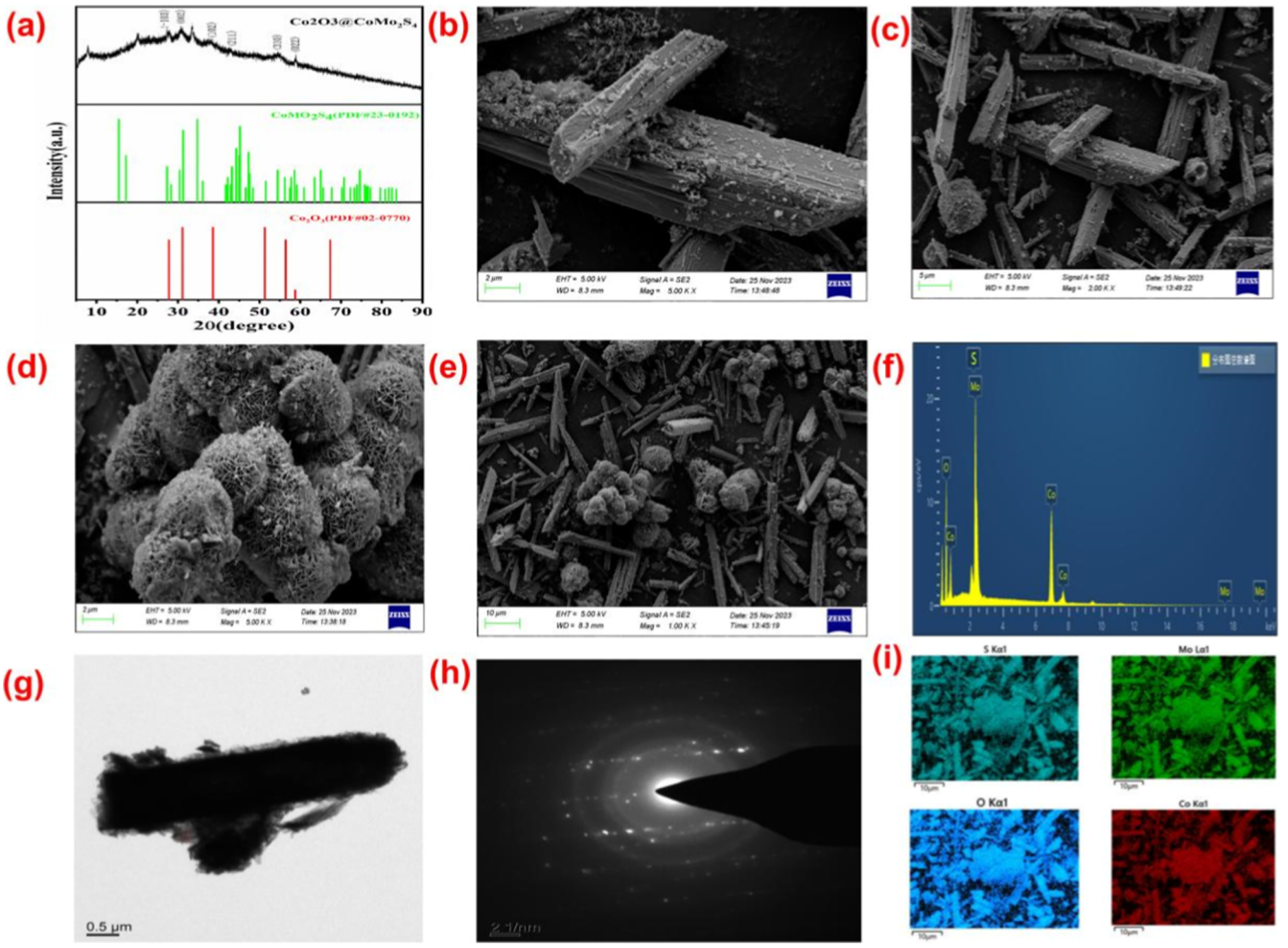

Figure 2. (a) XRD patterns of Co_2O_3@$CoMo_2S_4$. (b−e) SEM of Co_2O_3@$CoMo_2S_4$. (f) Energy-dispersive spectrometry (EDS) of Co_2O_3@$CoMo_2S_4$. (g) TEM of Co_2O_3@$CoMo_2S_4$. (h) Selected area electron diffraction (SAED) of Co_2O_3@$CoMo_2S_4$. (i) Elemental mapping.

py, were employed to evaluate the performance of the Co_2O_3@$CoMo_2S_4$//AC asymmetric supercapacitor. The Co_2O_3@$CoMo_2S_4$//AC supercapacitor achieves an energy density of 41.66 Wh kg^{-1} and a power density of 0.35 kW kg^{-1}.

2. EXPERIMENTS

2.1. Synthesis of Co_2O_3@$CoMo_2S_4$. Figure 1 depicts a diagram illustrating the creation of Co_2O_3@$CoMo_2S_4$. All

https://doi.org/10.1021/acsomega.4c05172
ACS Omega 2025, 10, 8901−8910

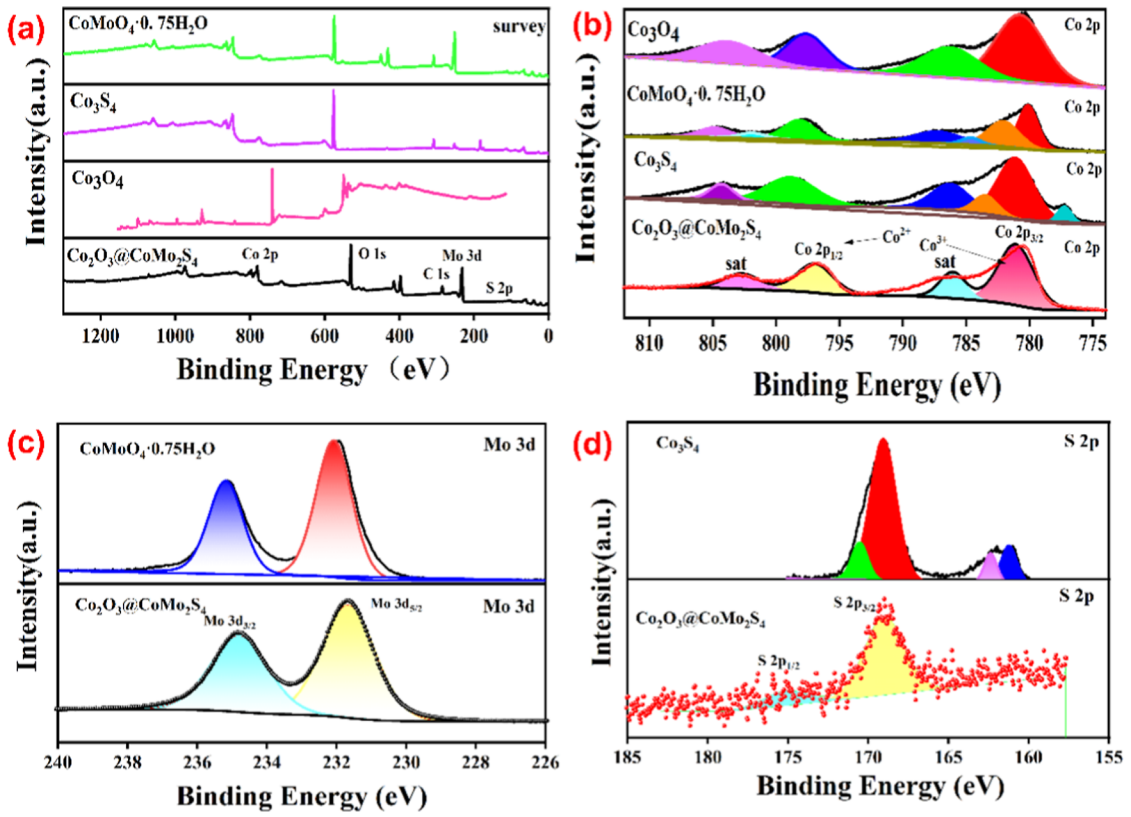

Figure 3. XPS of samples: (a) survey spectra. (b) High-resolution Co 2p spectra. (c) Mo 3 d. (d) S 2p.

reagents were bought and utilized in research without additional purification, and were commercially available in large quantities. A mixture was created by dissolving 0.01 M of cobalt chloride hexahydrate, 0.01 M of molybdenum trioxide, and 1 g of urea in 20 mL of purified water and then stirring to achieve a uniform solution. The Ni sheet, measuring 1 cm by 2 cm, was immersed in the solution after being cleaned. The mixture in a Teflon-lined stainless-steel autoclave was heated in an oven at 180 °C. After 6 h, the Ni-sheet and powder nanoparticles were extracted and washed three times with ethanol and deionized water to eliminate unreacted residues. Second, 0.4 g of sodium sulfide nonahydrate ($Na_2S{\cdot}9H_2O$), the previously obtained powder, and 0.5 g of urea were mixed into 60 mL of deionized water and stirred for 30 min to achieve a homogeneous solution. The solution was transferred into Teflon-lined stainless-cleaned 100 mL autoclave and maintained at 120 °C for 10 h. Once cooled to room temperature, the Ni-sheet and powder were repeatedly washed with ethanol and deionized water, respectively. The product was dried overnight at 60 °C.

Additionally, a Co_3O_4 sample was prepared without the inclusion of MoO_3, and a Co_3S_4 sample was also created by using the identical procedure. Meanwhile the $CoMoO_4$ sample was also prepared without adding $Na_2S{\cdot}9H_2O$.

2.2. Materials Characterizations and Electrochemical Measurements. The details of this part can be found in the Supporting Information.

3. RESULTS AND DISCUSSION

3.1. Morphology and Microstructure Analysis. The XRD examination was utilized to analyze the crystal formations of all synthesized composites. Figure 2 displays the pertinent XRD diffraction patterns. XRD pattern analysis indicated that the peaks of the synthesized Co_2O_3@$CoMo_2S_4$ aligned with the standard reference cards ($CoMo_2S_4$, PDF#23-0192 and Co_2O_3, PDF#02-0770), implying the formation of distinct core−shell structures. Specifically, diffraction peaks at 27.29°, 31.07°, 8.08°, 42.37°, 54.38°, and 58.81° were observed, indicating the presence of crystal plane families (−103), (002), (102), (211), (310), and (022), thus confirming the successful synthesis of Co_2O_3@$CoMo_2S_4$.

SEM was used for examining the structure of the items. Figure 2b−e illustrates the arrangement of Co_2O_3@$CoMo_2S_4$ on Ni foam. The surface morphology of Co_2O_3@$CoMo_2S_4$ was distinctively rough and uneven, characterized by numerous nanosheets attached to the cylindrical surface, forming a unique shell structure, as compared to other samples (Figures S1−S3). The core−shell design increases surface area, reactive sites, and shortens ion paths, reducing resistance in the electrode.[38−40] Figure 2f,i shows the mappings conducted by the EDS that further confirms the basic structure of the composite material. Figure 2g,h presents the high-resolution TEM image and the SAED pattern of Co_2O_3@$CoMo_2S_4$, respectively. As displayed in Figure 2g, the unique nanorod nanosheet core−shell structures were clearly revealed. The SAED pattern revealed diffraction rings with bright spots, indicating the polycrystalline nature of the material (Figure 2h). The core−shell nanostructures, with their increased specific surface area and abundance of electrochemical active sites, facilitated REDOX reactions, enhanced induced current generation, and improved electrochemical cycle stability.[41,42]

Figure 3 shows the XPS analysis of Co_2O_3@$CoMo_2S_4$, Co_3O_4, Co_3S_4, and $CoMoO_4{\cdot}0.75H_2O$ samples. A study was conducted to examine surface element composition and oxidation states to determine the chemical makeup. The XPS survey of the Co_2O_3@$CoMo_2S_4$ sample (Figure 3a) confirmed the presence

https://doi.org/10.1021/acsomega.4c05172
ACS Omega 2025, 10, 8901−8910

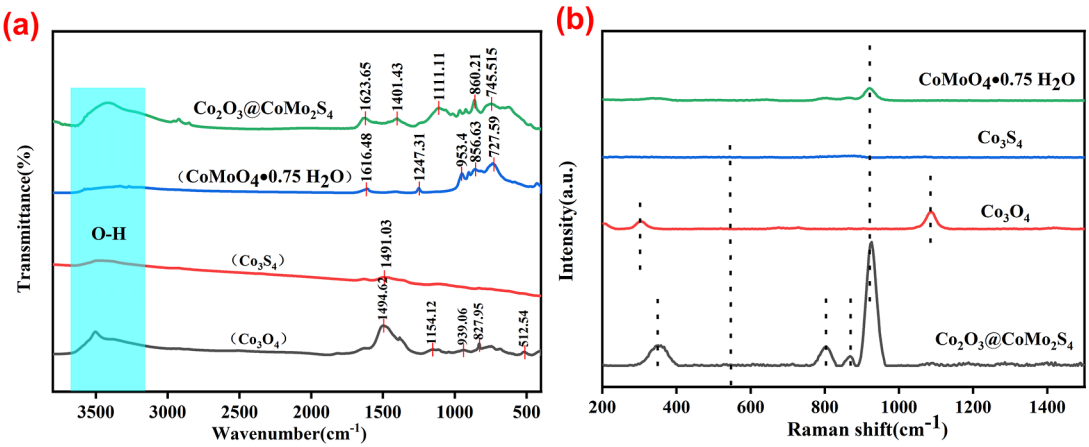

Figure 4. (a) FTIR spectra results. (b) Raman spectra results.

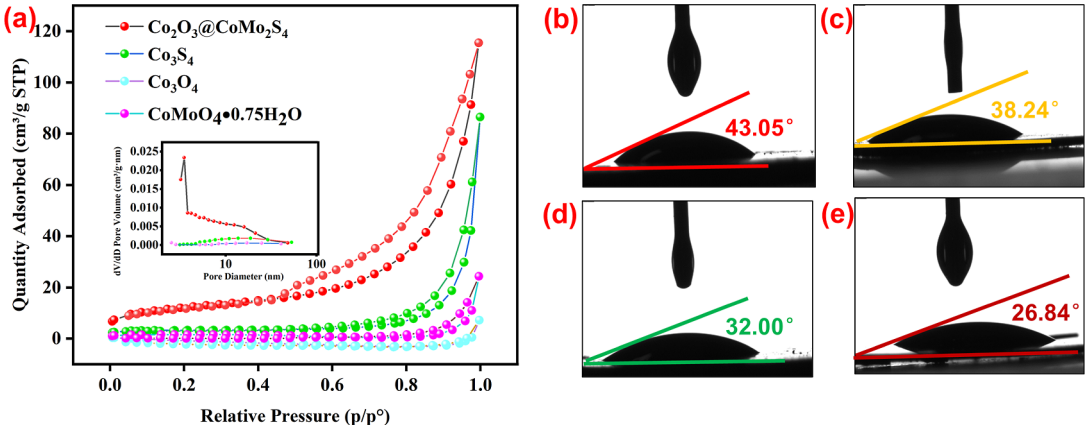

Figure 5. (a) Nitrogen adsorption−desorption isotherm. (b−e) KOH contact angle of the Co_3O_4, $CoMoO_4{\cdot}0.75H_2O$, Co_3S_4, and $Co_2O_3@CoMo_2S_4$.

of Co, Mo, S, C, and O elements. The Co 2p spectrum (Figure 3b) exhibited distinct peaks for Co $2p_{1/2}$ and Co $2p_{3/2}$ at binding energies of 796.85 and 781.25 eV, respectively, along with two satellite peaks labeled as Sat. The peaks at 802.9 and 786.1 eV were distinctive for Co^{2+} and Co^{3+} ions.[43] The Mo $3d_{5/2}$ and Mo $3d_{3/2}$ peaks were observed at approximately 231.7 and 234.85 eV, respectively, as shown in Figure 3c. Furthermore, the S $2p_{1/2}$ and S $2p_{3/2}$ peaks appeared at around 175.21 and 169.05 eV, respectively (Figure 3d), indicating metal−sulfur interactions and low-coordination sulfur ions on the surface, suggesting the presence of S2−.[44−47]

Figure 4a presents the FTIR spectra of $Co_2O_3@CoMo_2S_4$, Co_3O_4, Co_3S_4, and $CoMoO_4{\cdot}0.75H_2O$, highlighting broad, intense bands near 3500 cm^{-1} attributed to O−H stretching vibrations from water molecules and hydrogen-bonded OH groups. Peaks at ∼1401, ∼1247, and 747 cm^{-1} correspond to Mo−O−Co and Mo−S−Co vibrations.[48,49] The $Co_2O_3@CoMo_2S_4$ composite shows similar peaks with slight shifts, indicating interactions between $CoMo_2S_4$ and Co_2O_3.

Raman spectroscopy (Figure 4b) identified key vibrational modes:[37] a peak at 354.70 cm^{-1} in $Co_2O_3@CoMo_2S_4$ related to Co_2O_3 vibrations[50] and another around 926 cm^{-1} associated with $CoMo_2S_4$ and $CoMoO_4$.[51] Shifts in the peaks for Co_3S_4, Co_3O_4, and $CoMoO_4$ in $Co_2O_3@CoMo_2S_4$ suggest defects from Co_2O_3 integration. Additional peaks around 800 and 869 cm^{-1} point to defect-induced S atom motions.[52]

The BET test characterized the pore size and specific surface area of $Co_2O_3@CoMo_2S_4$, Co_3O_4, Co_3S_4, and $CoMoO_4{\cdot}0.75H_2O$ composites. Each sample exhibited typical type-IV behavior in the N_2 adsorption and desorption isotherms, along with an H3-type hysteresis loop, which suggests the existence of mesopores.[53] The $Co_2O_3@CoMo_2S_4$ sample exhibited the highest specific surface area of 42 $m^2\ g^{-1}$ among those listed in Table S1. The $Co_2O_3@CoMo_2S_4$ composites were engineered with an advanced core−shell structure, enhancing specific surface area and increasing reactive sites. In Figure 5a, the inset displays the distributions of pore sizes for the composites $Co_2O_3@CoMo_2S_4$, Co_3O_4, Co_3S_4, and $CoMoO_4{\cdot}0.75H_2O$. The $Co_2O_3@CoMo_2S_4$ composites contain a variety of hierarchical pores, ranging from micropores to macropores. Micropores offered extra reactive locations, while mesopores enhanced the speed of electrolyte ion diffusion, and macropores established effective routes for ion transportation.[54] The layered porous configuration of the $Co_2O_3@CoMo_2S_4$ compounds can significantly enhance their electrochemical efficiency.

Additionally, the $Co_2O_3@CoMo_2S_4$ specimen undergoes a notable decrease in the KOH contact angle, decreasing from 43.05° to 26.84° after KOH activation. In Figure 5b−e, the $Co_2O_3@CoMo_2S_4$ sample demonstrates enhancements in surface hydrophilicity and electrolyte accessibility.

3.2. Electrochemical Analysis. The prepared samples were evaluated for electrochemical performance using a three-electrode setup with 6 M KOH as the electrolyte. Figure 6a illustrates the CV curves for $Co_2O_3@CoMo_2S_4$, Co_3O_4, Co_3S_4, and $CoMoO_4{\cdot}0.75H_2O$ electrodes at a scan rate of 50 mV s^{-1}. The $Co_2O_3@CoMo_2S_4$ material demonstrates superior electro-

https://doi.org/10.1021/acsomega.4c05172
ACS Omega 2025, 10, 8901−8910

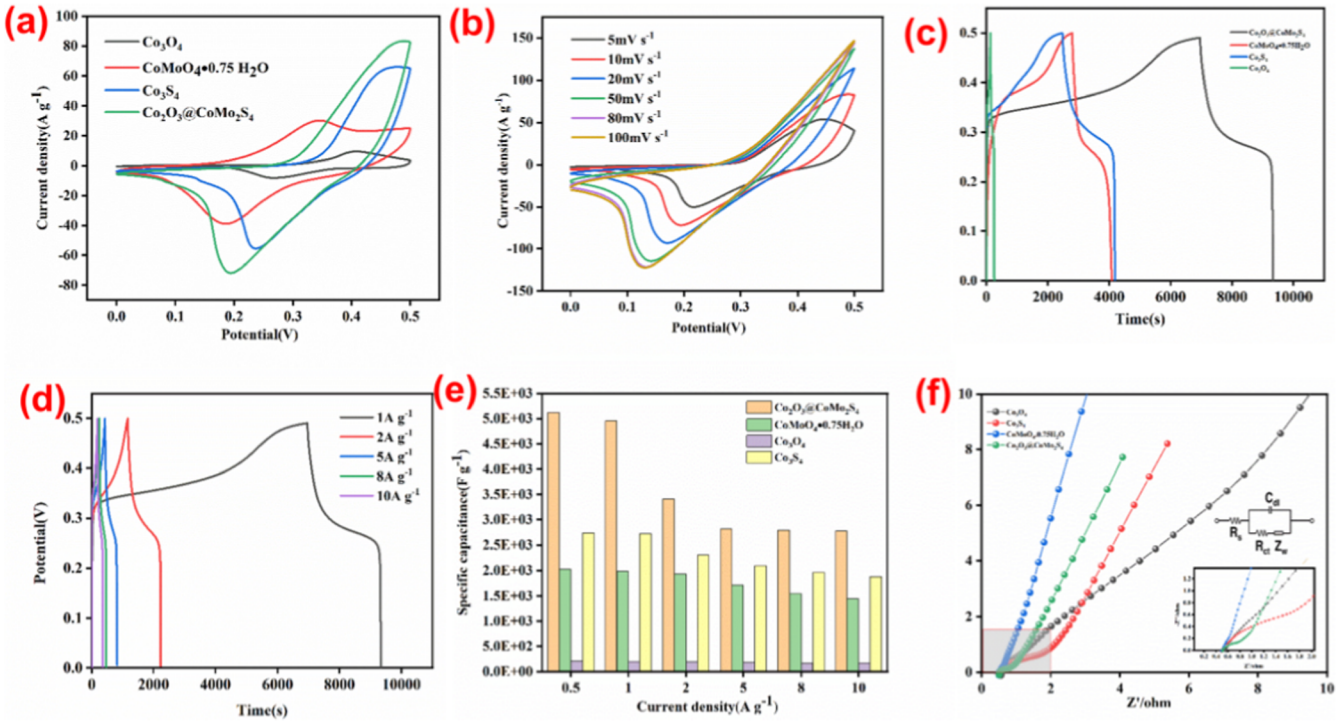

Figure 6. Electrochemical measurements of Co_2O_3@$CoMo_2S_4$, Co_3O_4, Co_3S_4, and $CoMoO_4$·$0.75H_2O$ in 6 M KOH. (a) Comparison of CV curves at the scan rate of 10 mV s^{-1}. (b) CV plots at different scan rates. (c) GCD curves at the current density of 1 A g^{-1}. (d) GCD plots at different current densities of Co_2O_3@$CoMo_2S_4$. (e) Specific capacitance at various current densities. (f) EIS curves of Co_2O_3@$CoMo_2S_4$, Co_3O_4, Co_3S_4, and $CoMoO_4$·$0.75H_2O$.

chemical performance, as evidenced by its larger CV curve area and higher redox peak intensity compared to other electrode materials. In Figure 6b, the peak potential of the anode/cathode may shift toward positive or negative directions with changes in the scan rates of Co_2O_3@$CoMo_2S_4$ cyclic voltammetry curves, due to constraints in ion diffusion/transfer kinetics at higher scan rates as mentioned in[55].

The discharge graphs at a current density of 1 A g^{-1} (Figure 6c) clearly demonstrate the improved energy storage capacity. The discharge plateau of the Co_2O_3@$CoMo_2S_4$ electrode is notably longer than that of other samples, providing further evidence of its superior capacity. Figure 6d presents the galvanostatic charge−discharge curves for Co_2O_3@$CoMo_2S_4$ electrode materials across different current densities, while Figure 6e shows the specific capacitance of hybrid electrodes Co_2O_3@$CoMo_2S_4$, Co_3O_4, Co_3S_4, and $CoMoO_4$·$0.75H_2O$ at various densities. The Co_2O_3@$CoMo_2S_4$ electrode demonstrates specific capacitances between 5123.5 and 2780.4 F g^{-1} across different current densities. The electrode materials' enhanced specific capacitance is attributed to four factors, (1) including the direct growth on nickel foam, which enhances surface area and minimizes ion and electron diffusion lengths. (2) This direct growth method removes excess materials, avoids "dead volume," and speeds up redox reactions. (3) No additives like graphene or binders are used, reducing internal resistance and improving conductivity.[41] (4) The unique structure and oxygen content of Co_2O_3@$CoMo_2S_4$ contribute to its higher specific capacity compared to Co_3O_4, Co_3S_4, and $CoMoO_4$·$0.75H_2O$. The uniform active site distribution in Co_2O_3@$CoMo_2S_4$ accelerates charge/ion transfer, enhancing double-layer capacitance and conductivity.[40] The residual oxygen-containing functional groups on Co_2O_3@$CoMo_2S_4$ contribute to the Faradaic redox capacitance. However, a high scan rate may impede the diffusion of electrolyte ions to the inner surface of the active material, leading to a decrease in specific capacity.

Figure 6f presents the Nyquist diagrams from the EIS test, comparing Co_2O_3@$CoMo_2S_4$ with Co_3O_4, Co_3S_4, and $CoMoO_4$·$0.75H_2O$ across a frequency range that encompasses high-frequency regions and the electrical equivalent circuit. The calculated Rs values for these samples are consistent with the electrode setup and electrolyte used. In the high-frequency region, all samples display small semi circles, indicating low charge transfer resistance. Co_2O_3@$CoMo_2S_4$ (Rct = 0.105 Ω) has a lower Rct value than the others (Rct Co_3O_4 = 1.08 Ω, Rct Co_3S_4 = 0.211 Ω, Rct $CoMoO_4$·$0.75H_2O$ = 0.328 Ω), suggesting the least resistance to charge transfer related to the curvature diameter.[56] Co_2O_3@$CoMo_2S_4$ shows the most significant slope in the lower frequency range compared to the other samples, implying reduced Warburg impedance due to electrolyte ion diffusion at the electrode surface.[57] In essence, Co_2O_3@$CoMo_2S_4$ demonstrates exceptional charge and ion transfer capabilities. Therefore, the EIS analysis confirms that Co_2O_3@$CoMo_2S_4$ has a higher reaction rate than the other samples when used as a supercapacitor electrode.

Analyzing cyclic voltammetry data at different scan rates is crucial for understanding the charge storage mechanism and reaction kinetics of the Co_2O_3@$CoMo_2S_4$ composite electrode. In most cases, the total capacitance of the electrode material can be categorized as either capacitive or diffusion-controlled electrochemical processes.[58,59] Formula 1[60] can qualitatively evaluate the main influence of the governing mechanism based on the power law.

$$i = a\nu^b \tag{1}$$

The maximum current (A) is denoted as i, with a and b serving as the variables, while ν represents the scan rate (mV s^{-1}). The

https://doi.org/10.1021/acsomega.4c05172
ACS Omega 2025, 10, 8901−8910

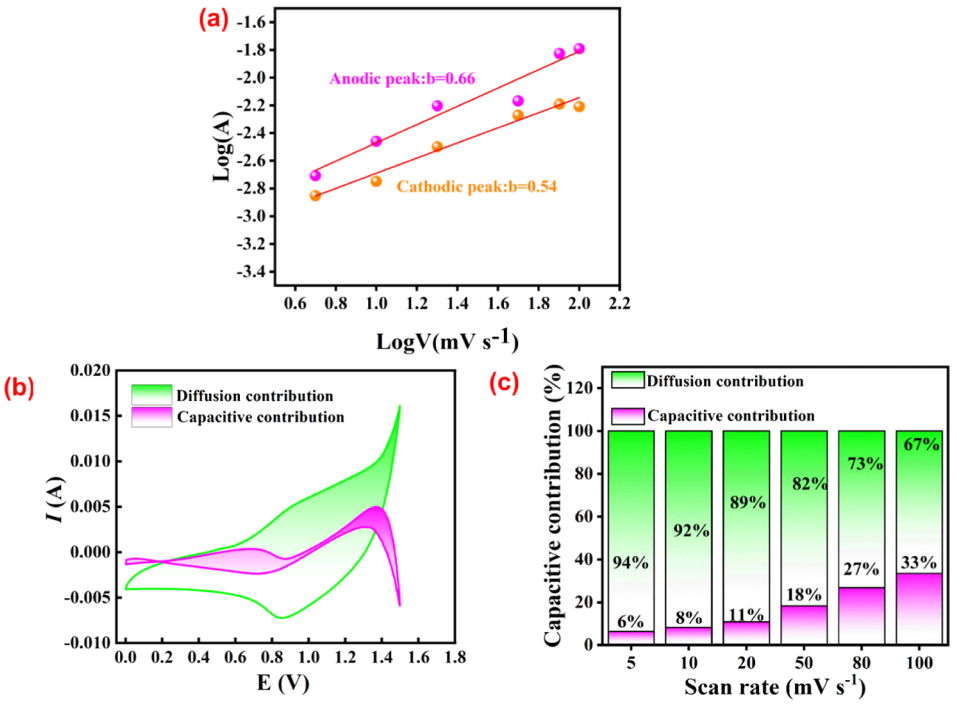

Figure 7. (a) Plots of log(peak current) (i) versus log(scan rate), (v). (b) Capacitance-confined (purple region) and diffusion-controlled (green region) contribution to charge storage of Co_2O_3@$CoMo_2S_4$ electrode at 10 mV s^{-1}. (c) Relative contribution of capacitance.

value of b can distinguish between different charge storage mechanisms of electrode materials. When b is below 0.5, the diffusion-controlled process prevails over the capacitive contribution. In the "transitional region" where b ranges from 0.5 to 1, the electrochemical process of composite electrodes is influenced by both diffusion-controlled and capacitive-controlled processes. When b exceeds 1, the primary factor is the process controlled by capacitance.[61] Formula 1 is then transformed into the subsequent formula 2.

$$\log i = \log a + b\log \nu \tag{2}$$

Figure 7a illustrates that the b value denotes the slope of the linear regression between log i and log ν. The Co_2O_3@$CoMo_2S_4$ composites electrode exhibits b values of 0.66 for anodic peaks and 0.54 for cathodic peaks, verifying the simultaneous existence of two methods for storing charges. Formulas 3 and 4[62] can be used to calculate the comparison of diffusion and capacitive contributions in the electrochemical process of the Co_2O_3@$CoMo_2S_4$ composites electrode.

$$i_\nu = k_1\nu + k_2\nu^{1/2} \tag{3}$$

$$i_\nu/\nu^{1/2} = k_1\nu^{1/2} + k_2 \tag{4}$$

When the voltage V is provided, adjustable constants k_1 and k_2 are used, with $k_1\nu$ representing the capacitive part and $k_2\nu^{1/2}$ representing the diffusion-controlled part.[63,64] The values of k_1 and k_2 can be determined by examining the plot of $i_\nu/\nu^{1/2}$ against $\nu^{1/2}$ at a given voltage using eq 4. These values are then represented by the slope and y-intercept of the curve. Subsequently, k_1 is used to calculate the capacitive component of the total capacitance based on eq 4. At a scan rate of 10 mV s^{-1}, the surface capacitive contribution accounts for 8% of the total area, as shown in the green shaded region of the CV curve (Figure 7b). The Co_2O_3@$CoMo_2S_4$ composites electrode's capacitive contribution ratios are outlined in Figure 7c. The contribution of surface capacitive effects to charge storage increases from 6% to 33% with higher scan rates. This is due to the decrease in ion diffusion time and the limited reaction at reactive sites with higher scan rates, resulting in a narrowing gap between the two charge storage mechanisms.[65,66]

An asymmetric supercapacitor was developed using Co_2O_3@$CoMo_2S_4$ as the cathode and AC as the anode, integrating Faradaic redox reactions with electrochemical double-layer energy storage mechanisms. Figure 8a illustrates the CV curves for Co_2O_3@$CoMo_2S_4$ and AC electrodes at a scanning rate of 50 mV s^{-1}. The optimal voltage for the Co_2O_3@$CoMo_2S_4$//AC asymmetric device was determined to be 0−1.4 V by maximizing the application window and accounting for polarization effects, combining the potential ranges of Co_2O_3@$CoMo_2S_4$ and AC. Figure 8b illustrates the alteration in the CV curve at 1.4 V, attributed to oxygen evolution and polarization. Figure 8c,d displays the CV and GCD plots of the asymmetric device Co_2O_3@$CoMo_2S_4$//AC, indicating that the primary energy storage mechanism involves Faradaic redox reactions.[12,13] The morphology of the CV remains consistent, showcasing the exceptional efficiency of this nonsymmetrical device even under a rapid scanning speed of 100 mV s^{-1}. According to eq S1 in Figure 8e, the Co_2O_3@$CoMo_2S_4$//AC asymmetric supercapacitor exhibits a specific capacity of 35.29 mAh g^{-1} at a current density of 1 A g^{-1}.

Simultaneously, formulas S2 and S3 were employed to determine power and energy density values. The Co_2O_3@$CoMo_2S_4$//AC asymmetric device shown in Figure 8f attains an energy density of 41.66 Wh kg^{-1} at a power density of 350 W kg^{-1}, attributed to its high specific capacity and broad operational voltage range. It maintains a capacity of 12.05 Wh kg^{-1} even under high power density conditions of 7000 W kg^{-1}. Electrochemical impedance spectroscopy (EIS) analysis verifies the superior reaction kinetics of the asymmetric supercapacitor electrode (Figure 8g). The experiment proves that the devices

https://doi.org/10.1021/acsomega.4c05172
ACS Omega 2025, 10, 8901−8910

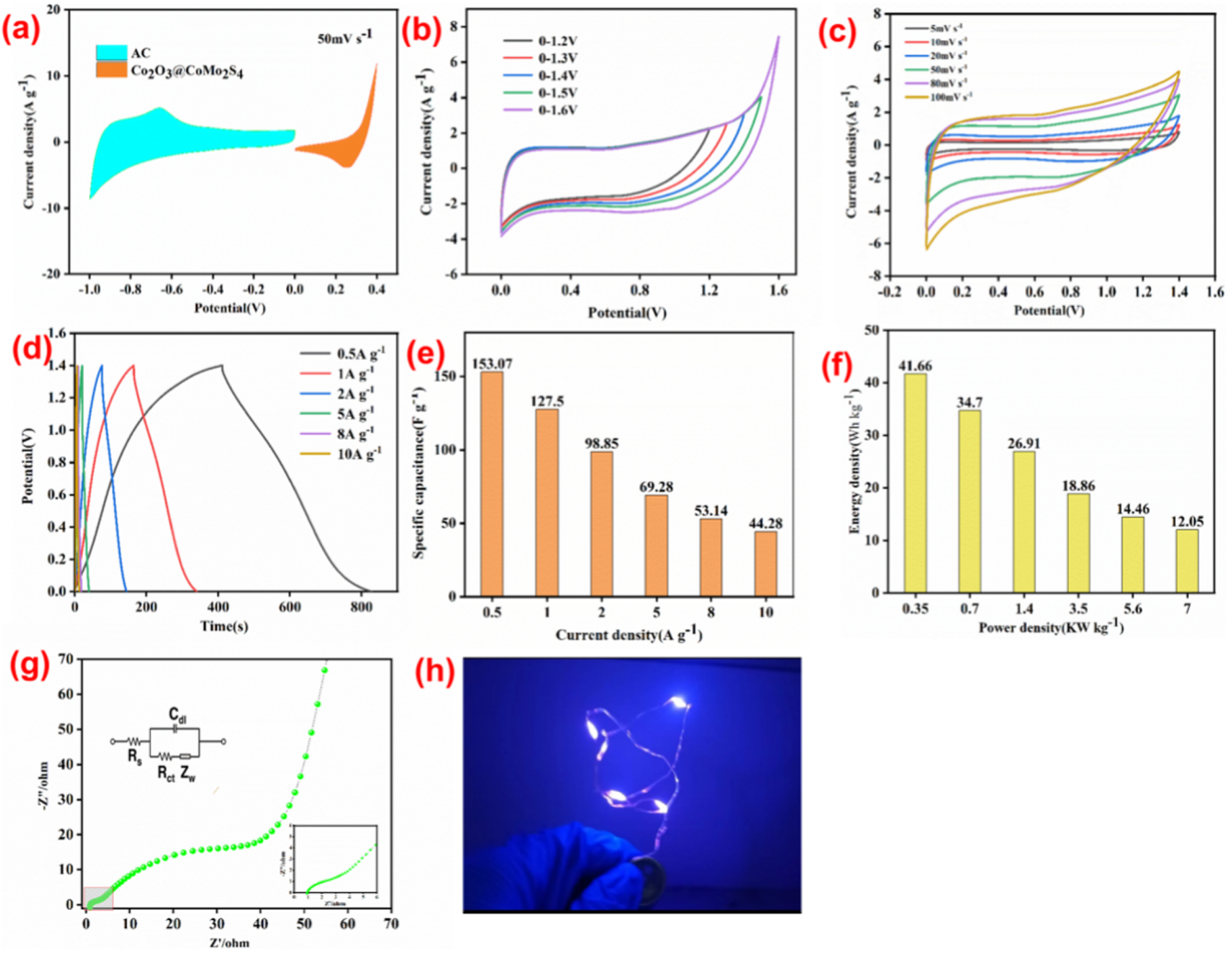

Figure 8. Electrochemical performance of the Co_2O_3@$CoMo_2S_4$//AC ASC device: schematic diagram representing the module of ASC device. (a) CV curves of the as-fabricated negative (AC, blue region) and positive (Co_2O_3@$CoMo_2S_4$, orange region) electrode at the scan rate of 50 mV s^{-1}. (b) CV profiles at diverse potential ranges at 50 mV s^{-1}. (c) CV profiles at different scan rates. (d) GCD profiles at different current densities. (e) Cs at different current densities. (f) Energy density at different power densities. (g) EIS curves. (h) Powering an LED light using a Co_2O_3@$CoMo_2S_4$//AC ASC device.

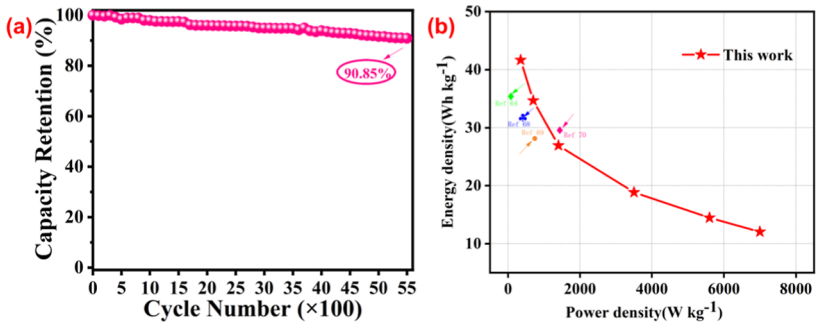

Figure 9. (a) Cyclic performance of the device at 2 A g^{-1}. (b) Ragone plot of Co_2O_3@$CoMo_2S_4$//AC.

can power red LEDs commonly used in commercial lighting applications (Figure 8h). This study clearly demonstrates the significant potential for practical real-world applications.

The cycle stability of the Co_2O_3@$CoMo_2S_4$//AC asymmetric supercapacitor was evaluated by measuring its capacity retention at a current density of 2 A g^{-1} (Figure 9a).The capacity retention after 5500 charge−discharge cycles was approximately 90.85% of the initial capacity, surpassing comparable asymmetric supercapacitors. The Co_2O_3@$CoMo_2S_4$//AC asymmetric supercapacitor exhibits exceptional long-term performance in practical applications, as evidenced by examples such as $CoMoS_4$//rGO (86% retention after 10,000 cycles),[65] $CoMo_2S_4$/NF-120//AC (80.1% retention after 10,000 cycles),[66] and $CoMoS_4$ @Ni−Co−S//AC (90.3% retention after 10,000 cycles).[67] The Ragone chart in Figure 9b demonstrates that supercapacitors can achieve a maximum

https://doi.org/10.1021/acsomega.4c05172
ACS Omega 2025, 10, 8901−8910

energy density of 41.66 Wh kg^{-1} at a power density of 0.35 kW kg^{-1}. The Co_2O_3@$CoMo_2S_4$///AC ASC device surpasses previously reported symmetrical and asymmetrical supercapacitors, such as $NiMoS_4$//AC (35 Wh kg^{-1}),[64] $CoMoO_4$//pureG (31.61 Wh kg^{-1}),[68] $NiCo_2S_4$//AC (28.8 Wh kg^{-1}),[69] and $CoMoS_4$//rGO[70] (27.2 Wh kg^{-1}) as shown in Table S2.

4. CONCLUSIONS

In summary, this study introduces an easy method for producing highly conductive Co_2O_3@$CoMo_2S_4$ composites through a hydrothermal process. The preprepared Co_2O_3@$CoMo_2S_4$ composites exhibit a core−shell structure with a large specific surface area, enhancing electron mobility during charge−discharge cycles and leading to excellent electrochemical performance. The uniform distribution of active sites within the core−shell structure enhances rapid charge and ion transfer, leading to improved electrochemical double layer capacitance and conductivity in metal sulfides. The Co_2O_3@$CoMo_2S_4$ core−shell structure exhibits a remarkable specific capacitance of 4951.8 F g^{-1} at 1 A g^{-1}, with outstanding cyclic stability of 90.85% after 5500 cycles, surpassing the performance of most reported bimetallic sulfides. The ASC device utilizing the Co_2O_3@$CoMo_2S_4$ composite as the anode attains an energy density of 41.66 Wh kg^{-1} at a power density of 350 W kg^{-1}. A comprehensive numerical analysis of diffusion and surface capacitance contributions is performed to investigate the charge storage mechanism. Undoubtedly, this synthesis approach offers a straightforward technique for creating bimetallic compound materials tailored for high-efficiency supercapacitors.

■ ASSOCIATED CONTENT

Supporting Information

The Supporting Information is available free of charge at https://pubs.acs.org/doi/10.1021/acsomega.4c05172.

Calculations of capacitance, energy density, and power density, along with characterization and electrochemical measurements; SEM analysis of Co_3O_4, $CoMoO_4$·$0.75H_2O$, and Co_3S_4, as well as BET analysis for Co_2O_3@$CoMo_2S_4$, Co_3O_4, $CoMoO_4$·$0.75H_2O$, and Co_3S_4; and energy density of the Co_2O_3@$CoMo_2S_4$//AC ASC device compared to previous research (PDF)

■ AUTHOR INFORMATION

Corresponding Authors

Huixin Jin − *College of Material and Metallurgy, Guizhou University, Guiyang, Guizhou 550025, PR China;* orcid.org/0000-0002-2714-3445; Email: hxjin@gzu.edu.cn

Yi Wang − *College of Chemistry and Material Engineering, Guiyang University, Guiyang, Guizhou 550005, PR China;* Email: wy742011@hotmail.com

Authors

Meilong Wang − *College of Material and Metallurgy, Guizhou University, Guiyang, Guizhou 550025, PR China*

Linsong Li − *College of Material and Metallurgy, Guizhou University, Guiyang, Guizhou 550025, PR China*

Zhentao Liu − *College of Material and Metallurgy, Guizhou University, Guiyang, Guizhou 550025, PR China*

Fuzhong Wu − *College of Material and Metallurgy, Guizhou University, Guiyang, Guizhou 550025, PR China;* orcid.org/0000-0002-2486-6605

Siyu Cai − *College of Chemistry and Material Engineering, Guiyang University, Guiyang, Guizhou 550005, PR China*

Complete contact information is available at: https://pubs.acs.org/10.1021/acsomega.4c05172

Author Contributions

M.W.: Conceptualization, Methodology, Software, Writing—Original Draft, Project administration; L.L. & Z.L.: Validation, Investigation; S.C. & F.W.: Resources; H.J. & Y.W.: Writing—Reviewing and Editing, Supervision.

Notes

The authors declare no competing financial interest.

■ ACKNOWLEDGMENTS

We acknowledge financial support from the National Natural Science Foundation of China (U24A2099, 52164036,52464054); Guizhou Key Laboratory of Advanced Low-Dimensional Green Energy Storage Materials in Universities[2022]056; the central government guides local science and technology development funds [2022]4053; the Natural Science Research Project of Guizhou Provincial Department of Education [2022]041; and the Research and Innovation Team for Water Ion Battery Materials in Higher Education Institutions in Guizhou Province[2023]081.

■ REFERENCES

(1) Shao, Y.; El-Kady, M. F.; Sun, J.; Li, Y.; Zhang, Q.; Zhu, M.; Wang, H.; Dunn, B.; Kaner, R. B. Design and mechanisms of asymmetric supercapacitors. *Chem. Rev.* **2018**, *118* (18), 9233−9280.

(2) Wang, F.; Wu, X.; Yuan, X.; Liu, Z.; Zhang, Y.; Fu, L.; Zhu, Y.; Zhou, Q.; Wu, Y.; Huang, W. Latest advances in supercapacitors: from new electrode materials to novel device designs. *Chem. Soc. Rev.* **2017**, *46* (22), 6816−6854.

(3) Lu, X. F.; Fang, Y.; Luan, D.; Lou, X. W. D. Metal-organic frameworks derived functional materials for electrochemical energy storage and conversion: a mini review. *Nano Lett.* **2021**, *21* (4), 1555−1565.

(4) Zhou, Y.; Qi, H.; Yang, J.; Bo, Z.; Huang, F.; Islam, M. S.; Lu, X.; Dai, L.; Amal, R.; Wang, C. H.; Han, Z. Two-birds-one-stone: multifunctional supercapacitors beyond traditional energy storage. *Energy Environ. Sci.* **2021**, *14* (4), 1854−1896.

(5) De Adhikari, A.; Morag, A.; Seo, J.; Kim, J. M.; Jelinek, R. Polydiacetyleneperylenediimide supercapacitors. *ChemSusChem* **2020**, *13* (12), 3230−3236.

(6) Han, X.; Chen, Q.; Zhang, H.; Ni, Y.; Zhang, L. Template synthesis of $NiCo_2S_4$/Co_9S_8 hollow spheres for high-performance asymmetric supercapacitors. *Chem. Eng. J.* **2019**, *368*, 513−524.

(7) Yan, X.; Guo, Q.; Huang, W.; Xiong, Y.; Jing, S.; Zhang, X.; Huang, F.; Ge, X. Conjugated supercapacitor with suppressed self-discharge constructed by pairs of prelithiated Nb_2O_5@C with optimized elemental and phase purity in the carbon shell. *Carbon Neutralization* **2023**, *2*, 300−309.

(8) Yan, X.; He, Y.; Liu, X.; Jing, S.; Guan, J.; Gao, W.; Ray, S.; Xiong, Y.; Li, T.; Ge, X. Deterministic Effect of the Solid-State Diffusion Energy Barrier for a Charge Carrier On the Self-Discharge of Supercapacitors. *ACS Energy Lett.* **2023**, *8* (5), 2376−2384.

(9) Theerthagiri, J.; Karuppasamy, K.; Durai, G.; Rana, A. S.; Arunachalam, P.; Sangeetha, K.; Kuppusami, P.; Kim, H. S. Recent advances in metal chalcogenides (MX; X = S, Se) nanostructures for electrochemical supercapacitor applications: a brief review. *Nanomaterials* **2018**, *8*, 256.

(10) Chakraborty, I.; Chakrabarty, N.; Senapati, A.; Chakraborty, A. K. CuO@NiO/Polyaniline/MWCNT Nanocomposite as High-Performance Electrode for Supercapacitor. *J. Phys. Chem. C* **2018**, *122*, 27180−27190.

(11) Liu, Z.; Li, L.; Wang, M.; Wu, F.; Jin, H.; Wang, Y. 3D hierarchical porous N, O co-doped carbon derived from the waste walnut shell via one-step carbonization for high-performance supercapacitor. *Electroanalysis* **2024**, *36*, No. e202400002.
(12) Ge, X.; Gu, C.; Yao, Z.; Sun, J.; Wang, X.; Tu, J. Pseudocapacitive material with 928 mAh cm^{-3} particle-level volumetric specific capacity enabled by continuous phase-transition. *Chem. Eng. J.* **2018**, *338*, 211−217.
(13) Ge, X.; Gu, C.; Yin, Z.; Wang, X.; Tu, J.; Li, J. Periodic stacking of 2D charged sheets: Self-assembled superlattice of Ni−Al layered double hydroxide (LDH) and reduced graphene oxide. *Nano Energy* **2016**, *20*, 185−193.
(14) Gao, Y.; Zhao, L. Review on recent advances in nanostructured transition-metalsulfide-based electrode materials for cathode materials of asymmetric supercapacitors. *Chem. Eng. J.* **2022**, *430*, 132745.
(15) Li, L. Y.; Xu, J.; Shi, M. J.; He, J.; Jiang, J. T.; Dai, K.; Jiang, Z. M.; Yan, C. In-situ Raman investigation and application of MXene-stabilized polypyrrole composite for flexible aqueous batteries. *Mater. Des.* **2022**, *217*, 110606.
(16) Chen, C.; Zhu, H. T.; Shi, M. J.; Hu, Li.T.; Xue, Z. Q.; Ye, H.; Zhao, L. P.; Yan, C. Oxygen vacancies-modulated tungsten oxide anode for ultra-stable and fast aqueous aluminum-ion storage. *Energy Storage Mater.* **2022**, *49*, 370−379.
(17) Li, K.; Teng, H.; Sun, Q.; Li, Y.; Wu, X.; Dai, X.; Wang, Y.; Wang, S.; Zhang, Y.; Yao, K.; Bao, Z.; Rao, J.; Zhang, Y. Engineering active sites on nitrogen-doped carbon nanotubes/cobaltosic oxide heterostructure embedded in biotemplate for high-performance supercapacitors. *J. Energy Storage* **2022**, *53*, 105094.
(18) Li, K.; Xiao, Y.; Zheng, T.; Sun, Q.; Zhang, Y.; Teng, H.; Wang, W.; Yao, K.; Rao, J.; Zhang, Y. Vanadium doping and phosphorus vacancy co-regulation of biotemplate derived three-dimensional cobalt phosphide to enhance pseudocapacitance performance. *Appl. Surf. Sci.* **2023**, *622*, 156950.
(19) Zhang, Z.; Zhang, X.; Xu, X.; Xiong, R.; Tian, X.; Wang, C. In-situ directly anchored CoMoS4 particles on reduced graphene oxide nanosheets for the high-efficiency asymmetric supercapacitor. *Colloids Surf., A* **2022**, *652*, 129762.
(20) Rani, B. J.; Pradeepa, S. S.; Hasan, Z. M.; Ravi, G.; Yuvakkumar, R.; Hong, S. I. Supercapacitor and OER activity of transition metal (Mo, Co, Cu) sulphides. *J. Phys. Chem. Solids* **2020**, *138*, 109240.
(21) Tang, Y.; Chen, T.; Yu, S.; Qiao, Y.; Mu, S.; Zhang, S.; Zhao, Y.; Hou, L.; Huang, W.; Gao, F. A highly electronic conductive cobalt nickel sulphide dendrite/quasispherical nanocomposite for a supercapacitor electrode with ultrahigh areal specific capacitance. *J. Power Sources* **2015**, *295*, 314−322.
(22) Ma, F.; Dai, X. Q.; Jin, J.; Tie, N.; Dai, Y. T. Hierarchical core-shell hollow $CoMoS_4$@ Ni-Co-S nanotubes hybrid arrays as advanced electrode material for supercapacitors. *Electrochim. Acta* **2020**, *331*, 135459.
(23) Du, J.; Li, K.; Qian, Y.; Yang, M.; Wang, H.; He, W.; Harnchana, V. Porous $NiCo_2S_4$ Networks as Electrodes for Electrochemical Supercapacitors. *Nano* **2016**, *11*, 1650133.
(24) Zhao, J.; Li, Z.; Zhang, M.; Meng, A.; Li, Q. Vertically cross-linked and porous $CoNi_2S_4$ nanosheets-decorated SiC nanowires with exceptional capacitive performance as a free-standing electrode for asymmetricsupercapacitors. *J. Power Sources* **2016**, *332*, 355−365.
(25) Xu, W.; Lu, J.; Huo, W.; Li, J.; Wang, X.; Zhang, C.; Gu, X.; Hu, C. Direct growth of $CuCo_2S_4$ nanosheets on carbon fiber textile with enhanced electrochemical pseudocapacitive properties and electrocatalytic properties towards glucose oxidation. *Nanoscale* **2018**, *10*, 14304−14313.
(26) Zhu, J.; Tang, S.; Wu, J.; Shi, X.; Zhu, B.; Meng, X. Wearable High-Performance Supercapacitors Based on Silver-Sputtered Textiles with $FeCo_2S_4$−$NiCo_2S_4$ Composite Nanotube-Built Multitripod Architectures as Advanced Flexible Electrodes. *Adv. Energy Mater.* **2017**, *7*, 1601234.
(27) Elshahawy, A. M.; Li, X.; Zhang, H.; Hu, Y.; Ho, K. H.; Guan, C.; Wang, J. Controllable $MnCo_2S_4$ nanostructures for high performance hybrid supercapacitors. *J. Mater. Chem. A* **2017**, *5*, 7494−7506.
(28) Zhang, K.; Zeng, H.-Y.; Li, H.-B.; Xu, S.; Lv, S.-B.; Wang, M.-X. Controllable preparation of $CuCo_2S_4$ nanotube arrays for high-performance hybrid supercapacitors. *Electrochim. Acta* **2022**, *404*, 139681.
(29) Jing, C.; Guo, X. L.; Xia, L. H.; Chen, Y. X.; Wang, X.; Liu, X. Y.; Dong, B. Q.; Dong, F.; Li, S. C.; Zhang, Y. X. Morphologically confined hybridization of tiny $CoNi_2S_4$ nanosheets into S, P co-doped graphene leading to enhanced pseudocapacitance and rate capability. *Chem. Eng. J.* **2020**, *379*, 122305.
(30) Ye, Y.; Yang, C.; Chen, P.; Ma, C.; Chen, X.; Guo, K. Thorn-like nanostructured $NiCo_2S_4$ arrays anchoring graphite paper as self-supported electrodes for ultrahigh rate flexible supercapacitors. *Electrochim. Acta* **2021**, *399*, 139420.
(31) Yang, Y. J.; Yao, C.; Chen, S.; Wang, N.; Yang, P.; Jiang, C.; Liu, M.; Cheng, Y. A 3D flower-like $CoNi_2S_4$/carbon nanotube nanosheet arrays grown on Ni foam as a binder-free electrode for asymmetric supercapacitors. *J. Electroanal. Chem.* **2021**, *888*, 115217.
(32) Tung, D. T.; Tam, L. T. T.; Dung, H. T.; Dung, N. T.; Hong, P. N.; Nguyet, H. M.; Van-Quynh, N.; Van Chuc, N.; Trung, V. Q.; Lu, L. T.; Minh, P. N. Freeze gelation 3D printing of rGO-$CuCo_2S_4$ nanocomposite for high performance supercapacitor electrodes. *Electrochim. Acta* **2021**, *392*, 138992.
(33) Xu, X.; Song, Y.; Xue, R.; Zhou, J.; Gao, J.; Xing, F. Amorphous $CoMoS_4$ for a valuable energy storage material candidate. *Chem. Eng. J.* **2016**, *301*, 266−275.
(34) Xu, X.; Liu, Q.; Liang, L.; Gu, H.; Zhao, Y.; Xing, X.; Zhang, X.; Hu, Y. Well-designed nanosheet-constructed porous $CoMoS_4$ arrays for ultrahigh-performance supercapacitors. *Ceram. Int.* **2020**, *46*, 4878−4888.
(35) Liu, H.; Zhao, D.; Hu, P.; Wu, X. Ternary core-shell structured transition metal chalcogenide for hybrid electrochemical capacitor. *Chin. Chem. Lett.* **2018**, *29*, 1799−1803.
(36) Yang, X.; Sun, H.; Zan, P.; Zhao, L.; Lian, J. Growth of vertically aligned Co_3S_4/$CoMo_2S_4$ ultrathin nanosheets on reduced graphene oxide as a high-performance supercapacitor electrode. *J. Mater. Chem. A* **2016**, *4*, 18857−18867.
(37) Nwaji, N.; Kang, H.; Goddati, M.; Tufa, L. T.; Gwak, J.; Sharan, A.; Singh, N.; Lee, J. Sulphur vacancy induced Co_3S_4@$CoMo_2S_4$ nanocomposites as a functional electrode for high performance supercapacitors. *J. Mater. Chem. A* **2023**, *11*, 3640−3652.
(38) Li, X.; Deng, R.; Li, Q.; Lin, D.; Wei, X.; Liu, X.; Jiang, N.; Huo, Y.; Xie, F.; Zheng, Q. Metal-Organic Framework-Derived ZnSe- and Co0.85Se-Filled Porous Nitrogen- Doped Carbon Nanocubes Interconnected by Reduced Graphene Oxide for Sodium- Ion Battery Anodes. *Inorg. Chem.* **2021**, *60*, 11693−11702.
(39) Gurav, S. R.; Sawant, S. A.; Chodankar, G. R.; Shembade, U. V.; Moholkar, A. V.; Sonkawade, R. G. Exploration of aqueous electrolyte on the interconnected petal-like structure of Co-MOFs for high-performance paper-soaked supercapacitors. *Electrochim. Acta* **2023**, *467*, 143027.
(40) Wang, M.; Li, L.; Liu, Z.; Wu, F.; Jin, H.; Wang, Y. Nanorod-like Bimetallic Oxide for Enhancing the Performance of Supercapacitor Electrodes. *ACS Omega* **2024**, *9*, 16118−16127.
(41) Lv, X.; Feng, L.; Lin, X.; Ni, Y. A novel 3D $MnNi_2O_4$@$MnNi_2S_4$ core-shell nano array for ultra-high capacity electrode material for supercapacitors. *J. Energy Storage* **2022**, *47*, 103579.
(42) Sekhar, S. C.; Ramulu, B.; Arbaz, S. J.; Hussain, S. K.; Yu, J. S. One-Pot Hydrothermal-Derived NiS_2−$CoMo_2S_4$ with Vertically Aligned Nanorods as a Binder-Free Electrode for Coin-Cell-Type Hybrid Supercapacitor. *Small Methods* **2021**, *5*, 2100335.
(43) Dai, Y.-H.; Kong, L.-B.; Yan, K.; Shi, M.; Zhang, T.; Luo, Y.-C.; Kang, L. Simple synthesis of a CoMoS4 based nanostructure and its application for high-performance supercapacitors. *RSC Adv.* **2016**, *6* (9), 7633−7642.
(44) Wei, M.; Wang, C.; Yao, Y.; Yu, S.; Liao, W.-H.; Ren, J.; Sun, R.; Wong, C.-P. Toward high-performance all-solid-state supercapacitors using facilely fabricated graphite nanosheet-supported $CoMoS_4$ as electrode material. *Chem. Eng. J.* **2019**, *355*, 891−900.

https://doi.org/10.1021/acsomega.4c05172
ACS Omega 2025, 10, 8901−8910

(45) Chen, H.; Jiang, J.; Zhang, L.; Wan, H.; Qi, T.; Xia, D. Highly conductive $NiCo_2S_4$ urchin-like nanostructures for high-rate pseudocapacitors. *Nanoscale* **2013**, *5*, 8879−8883.
(46) Guan, X.; Huang, M.; Yang, L.; Wang, G.; Guan, X. Facial design and synthesis of CoSx/Ni-co LDH nanocages with rhombic dodecahedral structure for highperformance asymmetric supercapacitors. *Chem. Eng. J.* **2019**, *372*, 151−162.
(47) Liu, H.; Zhang, M.; Ma, T.; Wang, Y.; Song, Z.; Wang, A.; Huang, Z. An enhanced capacitive storage of hybrid supercapacitor based on interconnected nitrogendoped graphene encapsulated honeycomb cobalt manganese pyrophosphate. *Chem. Eng. Sci.* **2021**, *238*, 116613.
(48) Sui, Y.; Ma, Y.; Gao, Y.; Song, J.; Ye, Y.; Niu, H.; Ma, W.; Zhang, P.; Qin, C. PANI/ MoO3-x shell−core composites with enhanced rate and cycling performance for flexible solid-state supercapacitors and electrochromic applications. *New J. Chem.* **2021**, *45* (24), 10654−10663.
(49) Zhang, X.; Zeng, X.; Yang, M.; Qi, Y. Investigation of a branchlike MoO(3)/ polypyrrole hybrid with enhanced electrochemical performance used as an electrode in supercapacitors. *ACS Appl. Mater. Interfaces* **2014**, *6* (2), 1125−1130.
(50) Liu, Y.; Xiao, C.; Lyu, M.; Lin, Y.; Cai, W.; Huang, P.; Tong, W.; Zou, Y.; Xie, Y. Ultrathin Co_3S_4 Nanosheets that Synergistically Engineer Spin States and Exposed Polyhedra that Promote Water Oxidation under Neutral Conditions. *Angew. Chem.* **2015**, *127*, 11383−11387.
(51) Xi, X.; Zeng, F.; Cao, H.; Cannilla, C.; Bisswanger, T.; de Graaf, S.; Pei, Y.; Frusteri, F.; Stampfer, C.; Palkovits, R.; Heeres, H. J. Enhanced C^{3+} alcohol synthesis from syngas using KCoMoSx catalysts: effect of the Co-Mo ratio on catalyst performance. *Appl. Catal., B* **2020**, *272*, 118950.
(52) Kang, L.; Zhang, M.; Zhang, J.; Liu, S.; Zhang, N.; Yao, W.; Ye, Y.; Luo, C.; Gong, Z.; Wang, C.; Zhou, X.; Wu, X.; Jun, S. C. Dualdefect Surface Engineering of Bimetallic Sulde Nanotubes towards Flexible Asymmetric Solid-state Supercapacitors. *J. Mater. Chem. A* **2020**, *8*, 24053−24064.
(53) Wang, E.; Jiang, S.; Bu, X. One-pot electrochemical assembling of porous cobalt hydroxide/nitrogen-doped porous graphene onto Ni foam as a binder-free electrode for supercapacitor applications. *J. Energy Storage* **2020**, *32*, 101881.
(54) Xu, X.; Song, Y.; Xue, R.; Zhou, J.; Gao, J.; Xing, F. Amorphous $CoMoS_4$ for a valuable energy storage material candidate. *Chem. Eng. J.* **2016**, *301*, 266−275.
(55) Adán-Más, A.; Silva, T. M.; Guerlou-Demourgues, L.; Bourgeois, L.; Labrugere-Sarroste, C.; Montemor, M. F. Nickel-cobalt oxide modified with reduced graphene oxide: performance and degradation for energy storage applications. *J. Power Sources* **2019**, *419*, 12−26.
(56) Acharya, J.; Ojha, G. P.; Kim, B. S.; Pant, B.; Park, M. Modish designation of hollowtubular rGO-$NiMoO_4$@Ni-Co-S hybrid core-shell electrodes with multichannel superconductive pathways for high-performance asymmetric supercapacitors. *ACS Appl. Mater. Interfaces* **2021**, *13* (15), 17487−17500.
(57) Lee, S.; Hwang, J.; Kim, D.; Ahn, H. Oxygen incorporated in 1T/2H hybrid MoS_2 nanoflowers prepared from molybdenum blue solution for asymmetric supercapacitor applications. *Chem. Eng. J.* **2021**, *419*, 129701.
(58) Choi, C.; Ashby, D. S.; Butts, D. M.; DeBlock, R. H.; Wei, Q. L.; Lau, J.; Dunn, B. Achieving high energy density and high-power density with pseudocapacitive materials. *Nat. Rev. Mater.* **2020**, *5* (1), 5−19.
(59) Naskar, P.; Maiti, A.; Chakraborty, P.; Kundu, D.; Biswas, B.; Banerjee, A. Chemical supercapacitors: a review focusing on metallic compounds and conducting polymers. *J. Mater. Chem. A* **2021**, *9* (4), 1970−2017.
(60) Chatterjee, D. P.; Nandi, A. K. A review on the recent advances in hybrid supercapacitors. *J. Mater. Chem. A* **2021**, *9* (29), 15880−15918.
(61) Zhao, X.; Ma, Q.; Tao, K.; Han, L. ZIF-derived porous $CoNi_2S_4$ on intercrosslinked polypyrrole tubes for high-performance asymmetric supercapacitors. *ACS Appl. Energy Mater.* **2021**, *4* (4), 4199−4207.
(62) Hao, Z.; He, X.; Li, H.; Trefilov, D.; Song, Y.; Li, Y.; Fu, X.; Cui, Y.; Tang, S.; Ge, H.; Chen, Y. Vertically aligned and ordered arrays of 2D MCo_2S_4@metal with ultrafast ion/electron transport for thickness-independent pseudocapacitive energy storage. *ACS Nano* **2020**, *14* (10), 12719−12731.
(63) Hu, P.; Liu, Y.; Liu, H.; Wu, X.; Liu, B. $MnCo_2O_4$ nanosheet/$NiCo_2S_4$ nanowire heterostructures as cathode materials for capacitors. *ACS Appl. Nano Mater.* **2021**, *4* (2), 2183−2189.
(64) Du, D.; Lan, R.; Humphreys, J.; Xu, W.; Xie, K.; Wang, H.; Tao, S. Synthesis of $NiMoS_4$ for High-Performance Hybrid Supercapacitors. *J. Electrochem. Soc.* **2017**, *164*, A2881−A2888.
(65) Xu, X.; Song, Y.; Xue, R.; Zhou, J.; Gao, J.; Xing, F. Amorphous $CoMoS_4$ for a valuable energy storage material candidate. *Chem. Eng. J.* **2016**, *301*, 266−275.
(66) Zhang, Y.; Guo, C.; Li, G.; Xu, L.; Guo, M. Construction of $CoMo_2S_4$ Nanorods/Nanosheets Electrodes with Enhanced Electrochemical Properties for Asymmetric Pseudocapacitors. *ChemPlusChem* **2022**, *87*, No. e202200180.
(67) Ma, F.; Dai, X.; Jin, J.; Tie, N.; Dai, Y. Hierarchical core-shell hollow $CoMoS_4$@Ni-CoS nanotubes hybrid arrays as advanced electrode material for supercapacitors. *Electrochim. Acta* **2020**, *331*, 135459.
(68) Sivakumar, P.; Raj, C. J.; R, R.; Kulandaivel, L.; Park, J.; Jung, H. Influence of heat-treatment temperature on the improvement of the electrochemical performance of $CoMoO_4$ nanomaterials for hybrid supercapacitor application. *Ceram. Int.* **2022**, *48* (19), 29018−29024.
(69) Ma, Z.; Sun, Z.; Jiang, H.; Li, F.; Wang, Q.; Qu, F. Nanoporous electrospun $NiCo_2S_4$ embedded in carbon fiber as an excellent electrode for high-rate supercapacitors. *Appl. Surf. Sci.* **2020**, *533*, 147521.
(70) Xu, X.; Song, Y.; Xue, R.; Zhou, J.; Gao, J.; Xing, F. Amorphous $CoMoS_4$ for a valuable energy storage material candidate. *Chem. Eng. J.* **2016**, *301*, 266−275.

https://doi.org/10.1021/acsomega.4c05172
ACS Omega 2025, 10, 8901−8910